JGR Space Physics

RESEARCH ARTICLE
10.1029/2019JA027445

Special Section:
Equatorial Aeronomy: New results from the 15th International Symposium on Equatorial Aeronomy (ISEA-15) and beyond

MELISSA: System description and spectral features of pre- and post-midnight *F*-region echoes

Fabiano S. Rodrigues[1], Weijia Zhan[1], Marco A. Milla[2], Bela G. Fejer[3], Eurico R. de Paula[4], Acacio C. Neto[4], Angela M. Santos[4], and Inez S. Batista[4]

[1]W. B. Hanson Center for Space Sciences, The University of Texas at Dallas, Richardson, TX, USA, [2]Radio Observatorio de Jicamarca, Instituto Geofisicio del Peru, Lima, Peru, [3]Utah State University, Logan, UT, USA, [4]Instituto Nacional de Pesquisas Espaciais, São José dos Campos, Brazil

Abstract Most of the low-latitude ionospheric radar observations in South America come from the Jicamarca Radio Observatory, located in the western longitude sector (~ 75°W). The deployment of the 30 MHz FAPESP-Clemson-INPE (FCI) coherent backscatter radar in the magnetic equatorial site of São Luis, Brazil, in 2001 allowed observations to be made in the eastern sector (~ 45°W). However, despite being operational for several years (2001–2012), FCI only made observations during daytime and pre-midnight hours, with a few exceptions. Here, we describe an upgraded system that replaced the FCI radar and present results of full-night *F*-region observations. This radar is referred to as Measurements of Equatorial and Low-latitude Ionospheric irregularities over São Luís, South America (MELISSA), and made observations between March 2014 and December 2018. We present results of our analyses of pre- and post-midnight *F*-region echoes with focus on the spectral features of post-midnight echoes and how they compare to spectra of echoes observed in the post-sunset sector. The radar observations indicate that post-midnight *F*-region irregularities were generated locally and were not a result of "fossil" structures generated much earlier in time (in other longitude sectors) and that drifted into the radar field-of-view. This also includes cases where the echoes are weak and that would be associated with decaying equatorial spread *F* (ESF) structures. Collocated digisonde observations show modest but noticeable *F*-region apparent uplifts prior to post-midnight ESF events. We associate the equatorial uplifts with disturbed dynamo effects and with destabilizing *F*-region conditions leading to ESF development.

Key Points:
- The MELISSA 30 MHz radar system is described and examples of *F*-region observations are introduced
- Results of the spectral analysis of pre- and post-midnight *F*-region echoes are presented and compared
- Results indicate the local development of *F*-region irregularities in the post-midnight sector

Correspondence to:
F. S. Rodrigues,
Fabiano@utdallas.edu

Citation:
Rodrigues, F. S., Zhan, W., Milla, M. A., Fejer, B. G., de Paula, E. R., Neto, A. C., et al. (2019), MELISSA: System description and spectral features of pre- and post-midnight F-region echoes. *Journal of Geophysical Research Space Physics Space Physics*, *124*. https://doi.org/10.1029/2019JA027445

Received 22 SEP 2019
Accepted 26 OCT 2019
Accepted article online 8 NOV 2019

1. Introduction

Equatorial spread *F* (ESF) is the general name often used when referring to the manifestation of electron density irregularities in the low-latitude ionosphere. ESF was first observed as diffuse radio echoes from the ionospheric F layer in the equatorial region (Booker & Wells, 1938). Since then, it has been studied theoretically and experimentally using different types of techniques (e.g. Woodman, 2009). Study of ESF is motivated by a better understanding of fundamental physical processes in the ionosphere-thermosphere (IT) system at low latitudes (e.g. Abdu, 2016). The study of ESF is also motivated by the impact of ESF irregularities on the performance of radio-based systems used for communication, navigation, and remote sensing (e.g. Basu et al., 1988; Carrano et al., 2012; Kintner et al., 2007).

It is well recognized that the so-called generalized Rayleigh-Taylor (GRT) instability is responsible for plasma structuring and ESF (Sultan, 1996; Zalesak et al., 1982). More recently, however, the collisional shear instability (CSI) was also proposed to play a role in ESF development and morphology (e.g. Aveiro & Hysell, 2010). The vertical plasma drift is one of the main drivers of the GRT instability, and the pre-reversal enhancement (PRE) of the drifts near sunset can explain most of the climatological features in ESF, including its high occurrence rate in the evening sector (Fejer et al., 1999; Huang & Hairston, 2015; Smith et al., 2016). Current research has focused on better understanding the sources of day-to-day variability in ESF development, including the sources of seed waves required for underlying instabilities (Abdu, 2019; Alam Kherani et al., 2009; Tsunoda et al., 2010). Another topic of current interest is related to better understanding of ESF events observed in the post-midnight sector (Candido et al., 2011; Yizengaw et al., 2013; Otsuka, 2018).

Significant advances in our understanding of ESF have come from incoherent and coherent backscatter radar observations made at the Jicamarca Radio Observatory (JRO) located near Lima, Peru, in the west-

ern American sector (e.g., Woodman & La Hoz, 1976; Hysell & Burcham, 2002). Coherent scatter radar (CSR) observations, in particular, have a number of advantages over other techniques for studies of *F*-region irregularities. Conventional, single-antenna CSR observations allows us to determine the height profile of ESF irregularities as a function of time. Conventional CSR observations also provide information about the Doppler velocity of the irregularities responsible for the echoes. Observations made with multiple antenna baselines and interferometric techniques can provide high resolution (in time and space) information about the two-dimensional (height versus zonal distance) distribution of irregularities within the radar field-of-view (e.g. Hysell & Chau, 2006; Harding & Milla, 2013; Rodrigues et al., 2017).

The success of the observations at Jicamarca led to the use of existing radar systems for ionospheric irregularity observations and to the deployment of new radar systems at various longitude sectors. For instance, Tsunoda et al. (1979) used a high-power, tracking radar (ALTAIR) located at the Kwajalein Atoll in the Marshal Islands (8.8° N, 167.5° E) to observe and study the evolution of ESF structures. The Middle and Upper atmosphere (MU) radar in Japan (34.8° N, 136.1° E) was also used for ionospheric studies and produced the first VHF radar observations of mid-latitude F-region irregularities (Fukao et al., 1988). In the Indian sector, the Gadanki MST radar (13.5°N, 79.2°E) was used to observe *F*-region irregularities associated with ESF (e.g. Patra et al., 1995). More recently, smaller radar systems have been deployed for dedicated ionospheric studies. For instance, Otsuka et al. (2009) reported results of continuous observations of *F*-region irregularities made by a 20-kW peak-power VHF radar system deployed in Kototabang (0.2°S, 100.3°E) in Indonesia. Ning et al. (2012) also reported the first observations of ionospheric irregularities made by a 24-kW peak power ionospheric radar deployed in Sanya, China (18.4°N, 109.6°E).

In the American sector radar observations were limited to Jicamarca (11.95°S, 76.87°W) for several decades. The 1994 NASA Guará rocket campaign led to temporary deployment and observations made with the 50 MHz CUPRI radar near the Alcantara rocket launching base (2.3°S, 44.4°W) in Brazil (Swartz & Woodman, 1998). In the late 1990s, the RESCO 50 MHz radar started operations but only made observations of *E*-region irregularities (Abdu et al., 2002). In 2001, the FAPESP-Clemson-INPE (FCI) 30 MHz radar was deployed and was capable of observing *E*- as well as *F*-region irregularities including those associated with 150-km echoes (de Paula & Hysell, 2004; Rodrigues et al., 2004).

While the FCI radar was capable of making observations of *F*-region echoes in the Brazilian sector, the observations were mostly limited to pre-midnight hours due to technical reasons. In 2014, an upgrade of the radar system was carried out, which allowed full-night observations and proper acquisition of the raw voltages for posterior analyses. The new system is referred to as Measurements of Equatorial and Low-latitude Ionospheric irregularities over São Luís , South America (MELISSA). In this report, we provide a description of the system and present and discuss results of ESF observations made by this radar, including those made during post-midnight hours. Additionally, we determine the spectral features of ESF echoes, which had not been investigated in previous radar observations in São Luís. More specifically, we compare the spectral features of post-midnight irregularity events with those of typical, pre-midnight ESF. We investigate the usefulness of the spectral features in distinguishing echoes caused by old ("fossil") *F*-region structures from those associated with new ("fresh") events, that is, structures generated near the radar site and around the time of the observations.

This report is organized as follows: In section 2, we describe the MELISSA radar system and the mode used for *F*-region observations. In section 3, we present examples of observations and discuss the main results of our analysis of pre- and post-midnight *F*-region echoes detected by MELISSA. Finally, in section 4, we summarize the main results and findings of this study.

2. Instrumentation, Observations, and Analysis

2.1. Instrumentation: MELISSA

The Measurements of Equatorial and Low-latitude Ionospheric irregularities over São Luís in South America (MELISSA) is a small, low-power 30 MHz coherent backscatter radar system deployed in São Luís, Brazil (2.59°S, 44.21°W, 3.25°S dip latitude). The design, deployment, and operation of this system is a scientific collaboration between the University of Texas at Dallas (UTD), the Brazilian National Institute for Space Research (INPE), and the Jicamarca Radio Observatory (JRO) in Peru. Figure 1 shows a map of South America and the location of São Luís. The isolines indicate the magnetic inclination of the geomagnetic field at 350 km altitude for March 2014. The location of Jicamarca Radio Observatory is also indicated for reference.

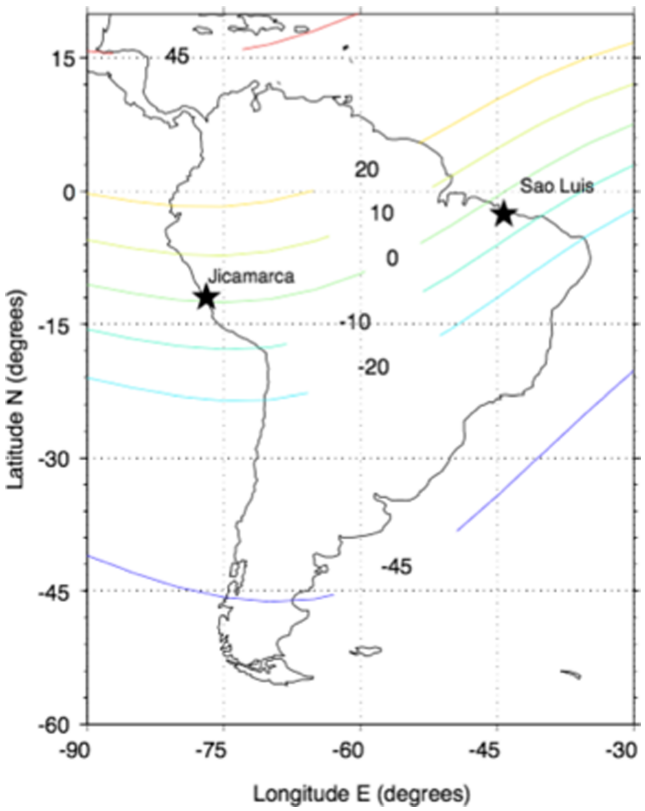

Figure 1. Map of South America showing the location of the São Luís site where the MELISSA radar system is located. The location of the Jicamarca Radio Observatory is also shown for reference.

The receiver of the MELISSA radar is formed by a digital acquisition system, a radar controller, and a DDS (direct digital synthesizer), which were developed at Jicamarca. MELISSA also uses a 16 kW peak power, dual output solid-state transmitter, which was designed and developed by ATRAD atmospheric radar systems. The transmitter allows a maximum duty cycle of 10%. The nominal operating frequency of the system is 29.795 MHz. MELISSA used the same antennas of the FCI radar system, previously deployed in São Luís (de Paula & Hysell, 2004). The antenna system is formed by four independent sets of antenna modules (or arrays) aligned in the zonal magnetic direction. Each module is formed by a 4×4 array of Yagi antennas. The HPBW (half-power beam width) of each module is approximately 16° in both EW (east-west) and NS (north-south) directions. Two modules are used for transmission while all the four modules are used for reception.

Having the four antenna arrays in full operation allowed interferometric imaging analyses to be done (Rodrigues et al., 2008). Unfortunately, for the period between 2014 and 2018, one and sometimes two antenna arrays were not operating due to technical issues. In this study, measurements from only one of the four antenna arrays are used. The study focuses on estimating the SNR (signal-to-noise ratio) of the echoes and identifying *F*-region irregularities associated with ESF. We also focus on estimating Doppler spectra for the measured echoes.

The main radar parameters used for *F*-region observations and analysis are listed in Table 1. Typically, the *F*-region mode started around sunset hours (~ 18:00 LT) and continued to make observations until morning the next day (~ 08:00 LT) for most weekdays. Gaps in the observations were caused by power outages, technical issues with the radar, and lack of operators.

2.2. Observations

Figure 2 shows an example of *F*-region observations made by MELISSA on 22 March 2014. It shows the Range-Time-Intensity (RTI) map of the observed echoes. This example serves to illustrate the coverage of the observations for one day, and the typical behavior of *F*-region echoes associated with a post-sunset equatorial

Table 1
Radar Parameters for the F-Region Observation Mode Used by MELISSA

Frequency	30 MHz
Peak Power	16 kW
IPP	1401.6 km
Code	28-bit
Baud length	2.4 km
Coherent integration	None
Number of FFT points	64
Number of FFT spectra averaged	25
Doppler Velocity	[−267 267] m/s

spread F (ESF) event. No echoes were observed in the post-midnight sector (00:00–08:00 LT) on this day. Cases of post-midnight echoes will be shown and discussed later on.

We have also created and examined the RTI maps for all the observations made between 2014 and 2018. Table 2 provides an overview of the number of observations made since 2014, and the number of observations when *F*-region echoes were visually identified in the RTI maps. Only cases when full pre-midnight (or full post-midnight) observations were available were considered for Table 2. For each season, we indicate the number of observations made during pre- and post-midnight hours. We also indicate the number of cases when *F*-region echoes were detected in each local time sector. The seasons are defined as March Equinox (February–April), June solstice (May–July), September Equinox (August–October), and December Solstice (November–January) and provide an estimate of measurements available throughout the year.

Table 2 shows that observations were not made continuously nor uniformly throughout all the seasons. This is, in most part, due to technical difficulties in the operation of the system, which requires human intervention, and the occurrence of power outages. Nevertheless, it can be seen that pre-midnight *F*-region echoes occur with significant occurrence rates during September and March Equinoxes and during December Solstice, which covers the ESF season in Brazil (Sobral et al., 2002). A significant number of observations were made in June solstice, but only a limited number of *F*-region echo events were identified in the RTI maps.

For the present study, we limit our spectral analyses to observations made during December Solstice 2015 when a significant number of both pre- and post-midnight ESF radar events were identified. Figure 3 presents RTI maps showing ESF irregularities observed during the selected period. The RTI maps on the left hand side column show examples of quiet-time pre-midnight events. To illustrate the behavior of typical ESF events, we only show cases when the geomagnetic Kp index did not exceed 3 for the day in consideration. The RTI maps on the right hand side column show all the post-midnight ESF events observed during Fall 2015.

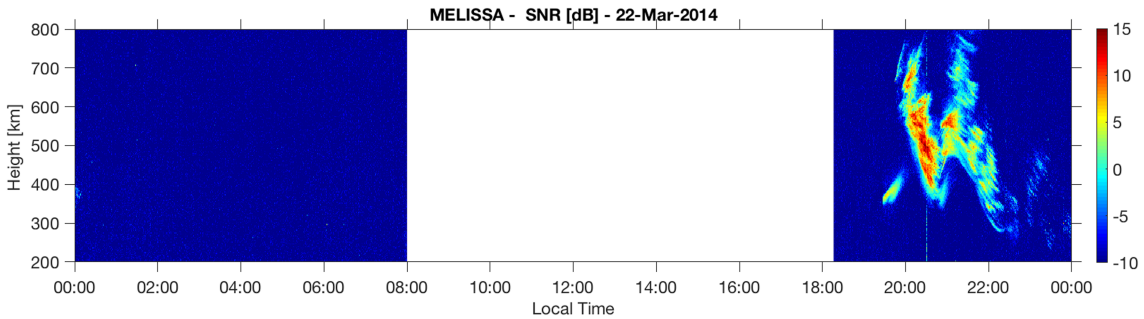

Figure 2. Range-Time-Intensity (RTI) showing an example of *F*-region observations made by MELISSA on 22 March 2014. The RTI map shows that F-region irregularities were not detected in the early nighttime hours (00:00-08:00 LT) but were observed in the post-sunset hours (18:00–24:00 LT).

Table 2
Summary of the F-Region Observations Made by MELISSA Between 2014 and 2018

Year	Mar. Equinox		Jun. Solstice		Sep. Equinox		Dec. Solstice	
	PRE	POST	PRE	POST	PRE	POST	PRE	POST
2014	20(19)	18(4)	22(8)	19(1)	8(2)	4(0)	N/A	N/A
2015	6(5)	7(0)	21(2)	27(1)	35(20)	36(2)	26(25)	25(8)
2016	23(16)	24(0)	38(6)	37(0)	46(27)	46(11)	15(14)	16(9)
2017	N/A	1(1)	N/A	N/A	26(14)	30(10)	21(17)	21(5)
2018	12(5)	12(3)	26(1)	20(0)	26(10)	24(6)	3(3)	5(4)

Note. The observations are grouped into seasons. Each season is subdivided into PRE- and POST-midnight observations. The first value in each group indicates the total number of observations, while the value in parentheses indicates the number of observations where echoes were identified. Finally, N/A indicates that observations were not available.

2.3. Spectral Analysis

We focus on determining features of the Doppler spectra of *F*-region echoes associated with pre- and post-midnight ESF observed by the 30 MHz MELISSA system. In order to analyze the features of the spectra, we determined two main parameters: the mean Doppler velocity ($\hat{v}$) and the mean spectral width (σ_v). These two spectral features are commonly used as indicators of the mean velocity and level of turbulence of the ionospheric irregularities within the volume illuminated by the radar (Hysell & Burcham, 2002; Patra et al., 1997; Woodman, 1985).

Doppler velocity spectra are obtained from the observed complex voltages using the FFT (Fast Fourier Transform) algorithm. As listed in Table 1, 64 points are used in the FFT estimates. Therefore, unaliased Doppler spectra with velocities between −267 and +267 m/s are obtained. Then, 25 Doppler spectra are averaged leading to a mean Doppler spectra every ∼15 s. Finally, the mean spectral velocity and width are obtained by least square fitting a Gaussian model to the measured spectra.

3. Results and Discussion

We now present additional details of the observations made by the MELISSA system. As mentioned earlier, we focus on presenting and discussing the spectral features of *F*-region echoes observed in the pre- and post-midnight sector.

We start by presenting and discussing an example that illustrates the behavior of the *F*-region echoes observed during a typical post-sunset ESF event (Figure 4) followed by examples of post-midnight events (Figures 5–8). We present and discuss the spectral features seen on three distinct types of post-midnight echo signatures identified in the RTI maps of December Solstice 2015 (see Figure 3). The RTI maps of the selected post-midnight examples represent the following cases: (a) *F*-region echoes detected near midnight (Figure 5). (b) Strong echoes detected in the post-midnight sector (Figures 6 and 7). The intensity of those echoes would suggest the detection of a new ("fresh") ESF event. Finally, we also show an example of (c) weak echoes detected during post-midnight hours (Figure 8). The weak echoes would suggest the detection of an old ("fossil") ESF event.

Also, in order to aid our presentation and discussion of the post-midnight observations we evaluated the behavior of the *F*-region over the radar site using collocated observations made by a digisonde. The variation of the virtual height of the *F*-layer base (h'F) and true height of the *F*-region peak (hmF2) are shown in Figure 9 for the example days of post-midnight ESF. The digisonde parameters are superimposed to the RTI maps.

3.1. Pre-Midnight *F*-Region Echoes

Figure 4 shows the first example of results obtained with our spectral analyses. It illustrates how the overall behavior of the spectra observed during a ESF post-sunset event (pre-midnight) event typically varies with time. The top panel shows the RTI map, from 18:00 LT to 24:00 LT, for the measurements made on the evening of 2 December 2015 when typical pre-midnight ESF event was detected. Echoes from four stages (times) of the ESF event have been selected based on the RTI map. The time and height for each of these

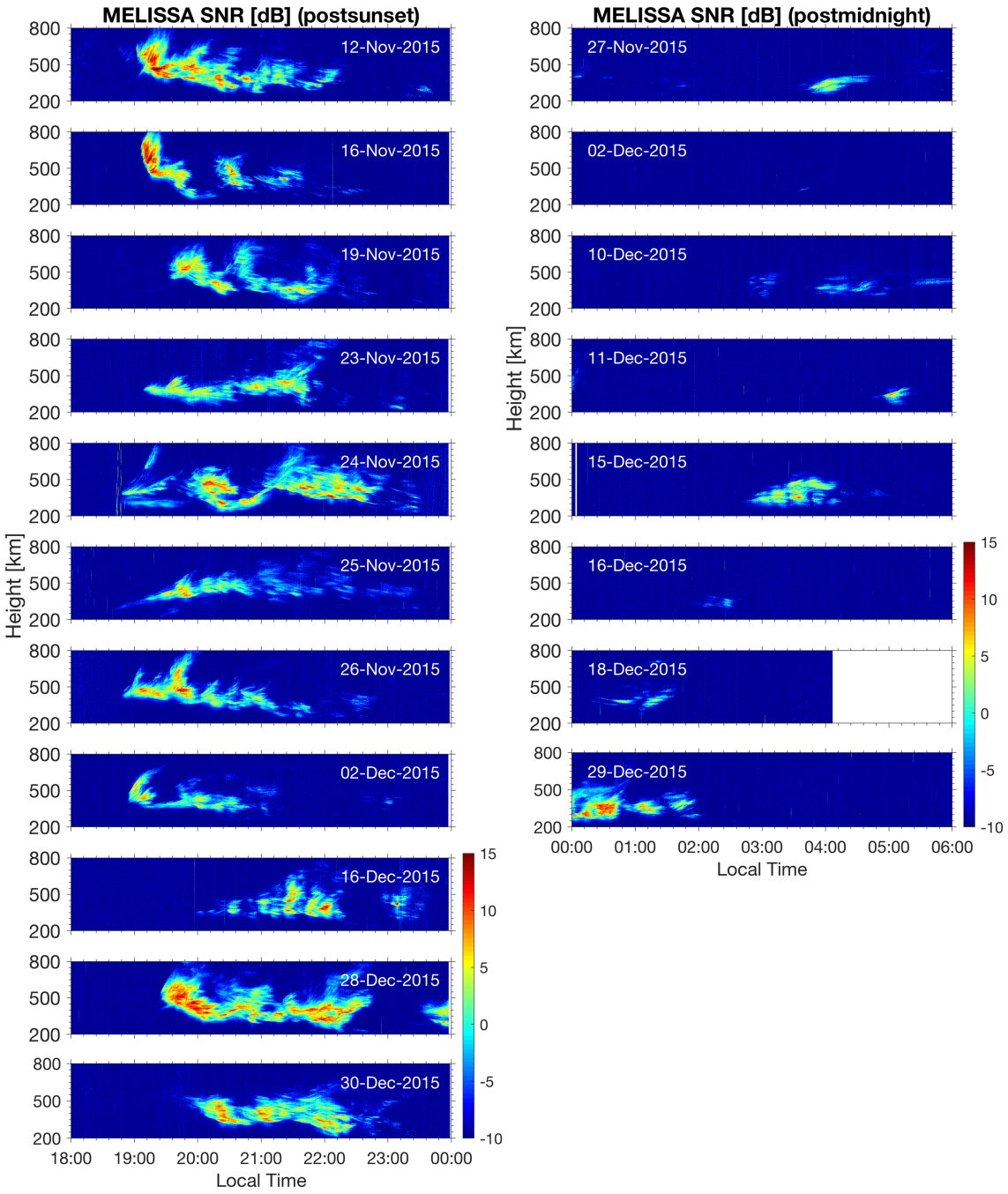

Figure 3. The panels on the left hand side show examples of RTI maps of post-sunset ESF events observed by MELISSA during December Solstice 2015. The panels on right hand side show the post-midnight events observed by MELISSA.

selections are indicated as markers (red stars) on the RTI map. Note that the selected heights were chosen based on echo intensity. Echoes with low SNR are too noisy for spectral analyses.

The first selection comes from a topside scattering layer (plume) observed around 19:00 LT. The second selection comes from what seems to be a second, smaller plume detected around 20:00 LT. The third selection comes from a third, late-night scattering structure observed around 20:30 LT. Finally, the fourth selection comes from the last observed bottomside echoes observed around 21:05 LT.

Below the RTI map, each column of panels shows three Doppler spectra for the selected regions described above. Doppler spectra for consecutive range gates are shown. The range gate heights are indicated on the

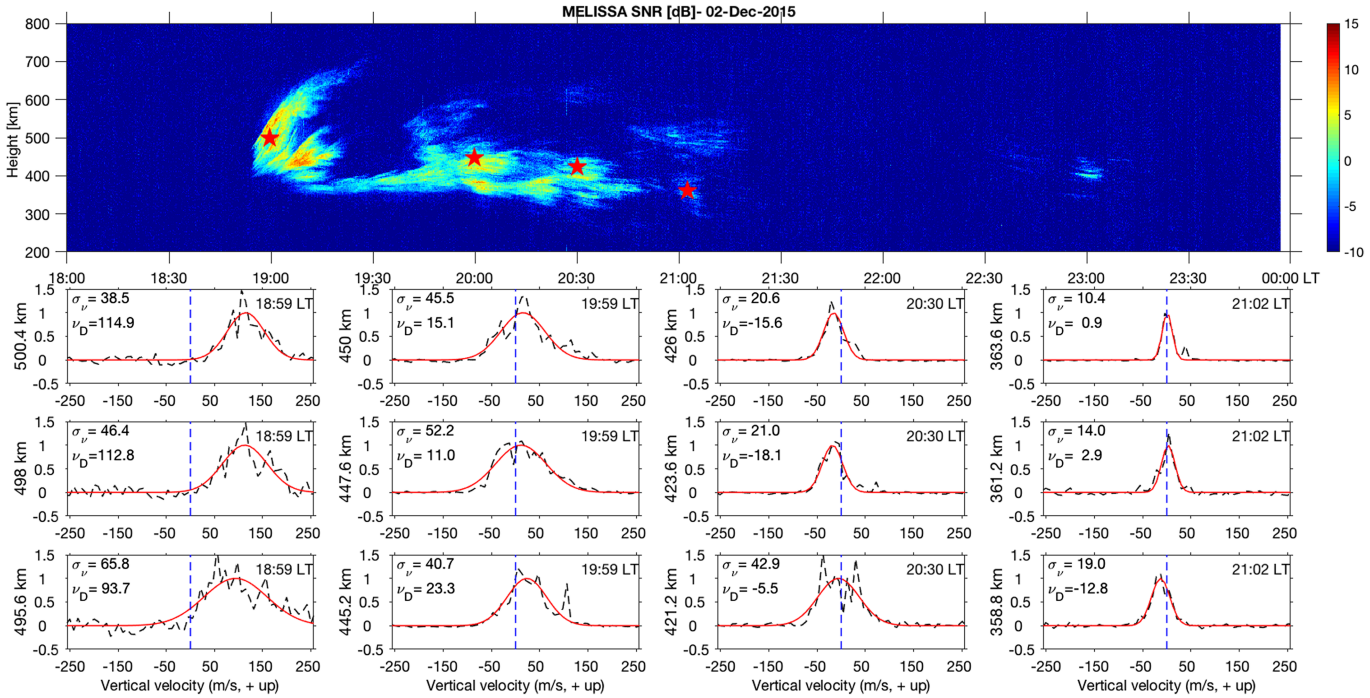

Figure 4. Top panel: Range-Time-Intensity (RTI) map of *F*-region echoes observed on 2 December 2015. Bottom panels: Each column shows examples of spectra observed at four different times during the irregularity event shown in the RTI map. Examples from three consecutive range gates are shown for each time. Times and heights are indicated in each panel and by markers (red stars) in the RTI map. Estimated mean Doppler velocities (v_D) and spectral widths (σ_v) are also provided in each panel (in m/s).

left hand side of each panel. The convention for the plots is that positive velocities indicate irregularities moving away from the radar (upward direction). The black dashed curves are the measured Doppler velocity spectra, and the red solid curves are the best-fit model results. The main parameters, mean Doppler velocity (v_D), and spectral width (σ_v) obtained from the fit routine are also indicated in each panel.

Figure 4 shows that echoes from the early evening plume have broad spectral widths and positive (upward) Doppler velocities. For the selected plume echoes, the widths vary between 38.5 and 65.8 m/s, and the mean velocities vary between 93.7 and 114.9 m/s. The spectral features vary noticeably from range gate to range gate and suggest a turbulent, upward flow of irregularities, which would be expected from the early, developing phase of ESF structures.

In our analyses of the spectra, we did not identify cases that could be affected by frequency aliasing, that is mean Doppler velocities that would exceed ~267 m/s. We found, however, cases where the Doppler spectrum does not follow the shape of a single Gaussian function. It has, instead, multiple peaks similar to observations made at Jicamarca (Woodman & La Hoz, 1976).

The second selection (second column of spectra) comes from a region of echoes that seemed to be caused by the passage of a second radar plume. In this case, however, the echoes have spectral widths that are comparable to or somewhat narrower than those observed during the first plume. The echoes continue to have positive mean Doppler velocities but with smaller amplitudes than those observed in the first case. The spectral widths now vary between 40.7 and 52.2 m/s, and the mean Doppler velocities vary between 11.0 and 23.3 m/s. The spectral features suggest the occurrence of a plume outside its main phase of development, older than the first plume but still evolving.

The third selection (third column of spectra) was from an echoing structure that is not as developed vertically as the first two cases. In this case, the spectral widths of the echoes are much narrower than those observed in the first plume, and the mean Doppler velocities are now negative indicating a downward mean flow of irregularities. The spectral widths vary between 21.0 and 42.9 m/s, and the mean Doppler velocities vary between −5.5 and −18.1 m/s. We interpret the spectral features as being those of a decaying ESF structure originated much earlier, presumably, to the west of the observation site.

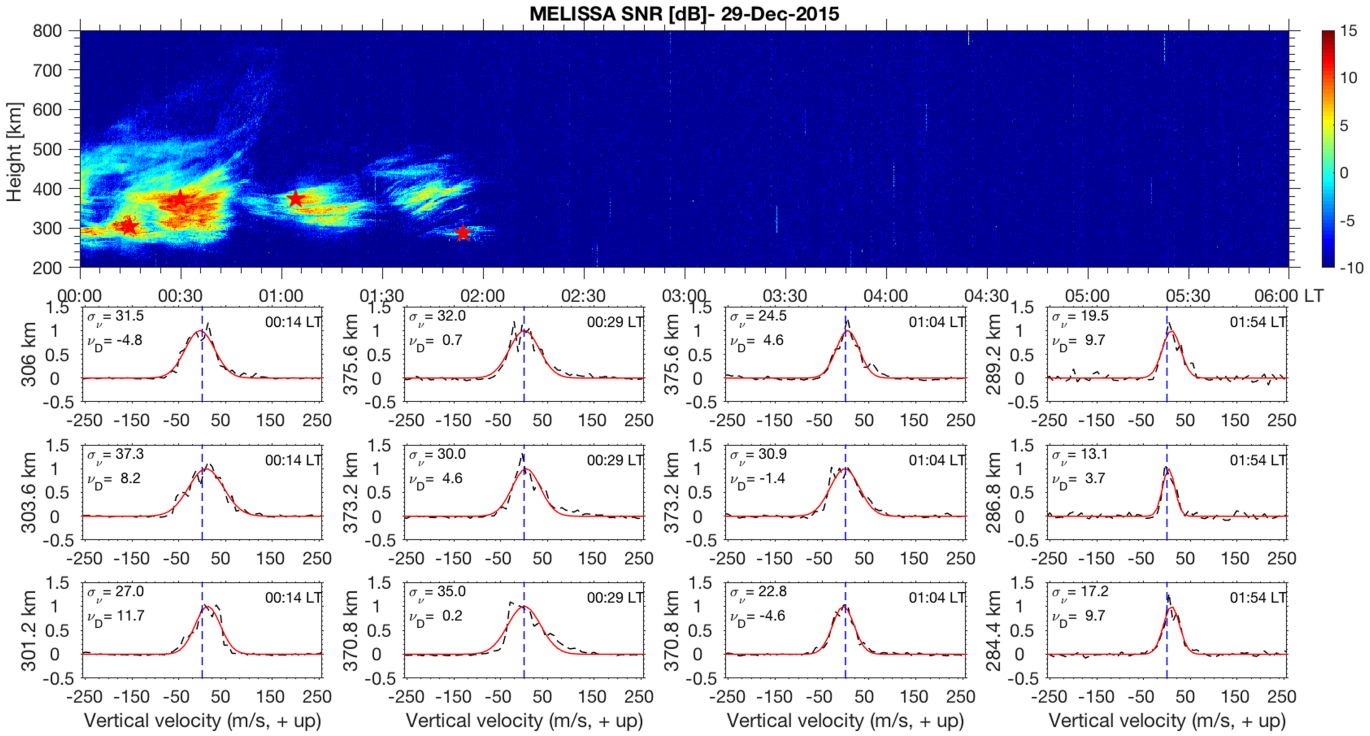

Figure 5. Same as Figure 4 but for 29 December 2015.

Finally, the last selection of echoes (fourth column of spectra) shows spectra that are, in general, very narrow and with negligible or negative (downward) mean Doppler velocities. Spectral widths vary between 10.4 and 19.0 m/s, and the mean Doppler velocities vary between 2.9 and −26.7 m/s. The spectral widths indicate reduced levels of turbulence. The occurrence of weak and negative mean Doppler velocities are interpreted as indicators of the background plasma flow, which is expected to be weak or downward around those times. Again, we associated these echoes to late-night, decaying ESF structures.

3.2. Post-Midnight *F*-Region Echoes

We now turn our attention to spectral features of *F*-region echoes observed in the post-midnight sector. As mentioned earlier, we selected a few cases that illustrate three different types of echoing layers detected during December Solstice 2015.

3.2.1. Near Midnight *F*-Region Irregularities

Figure 5 shows an example of post-midnight echoes that seemed to be the result of an ESF event that started in the pre-midnight sector and continued throughout midnight. Data presentation follows the same format of Figure 4. The post-midnight event was observed by MELISSA on 29 December 2015. Looking at Figure 3, we can see MELISSA observations for 28 December as well. These observations show that *F*-region echoes started to be observed around 19:30 LT on 28 December and ended at about 22:45 LT. Then they started again around 23:30 LT and continued throughout midnight producing the post-midnight echoes seen on 29 December (Figure 5).

Similar to Figure 4, the bottom panels of Figure 5 show the spectra of echoes selected from different times. The first two selections come from the region of intense echoes observed around 00:15 LT and 00:30 LT. The spectra show echoes with somewhat broad widths, between 27 and 37 m/s, and with small mean Doppler velocities. The spectra are broader than those of echoes observed late in the evening during typical ESF events. The spectral features combined with the intensity of the echoes (SNR ∼10 dB) indicate that the structures have recently developed. They resemble, for instance, the echoes observed around 20:00 LT in our first example of pre-midnight ESF (Figure 4).

The last two columns of spectra in Figure 5 show examples of echoes seen later at night, around 01:00 LT and 02:00 LT, respectively. Around 01:00 LT, echoes with moderate intensity are still observed, but the spectra have narrower widths than what was observed earlier. The mean Doppler velocities continue to be small.

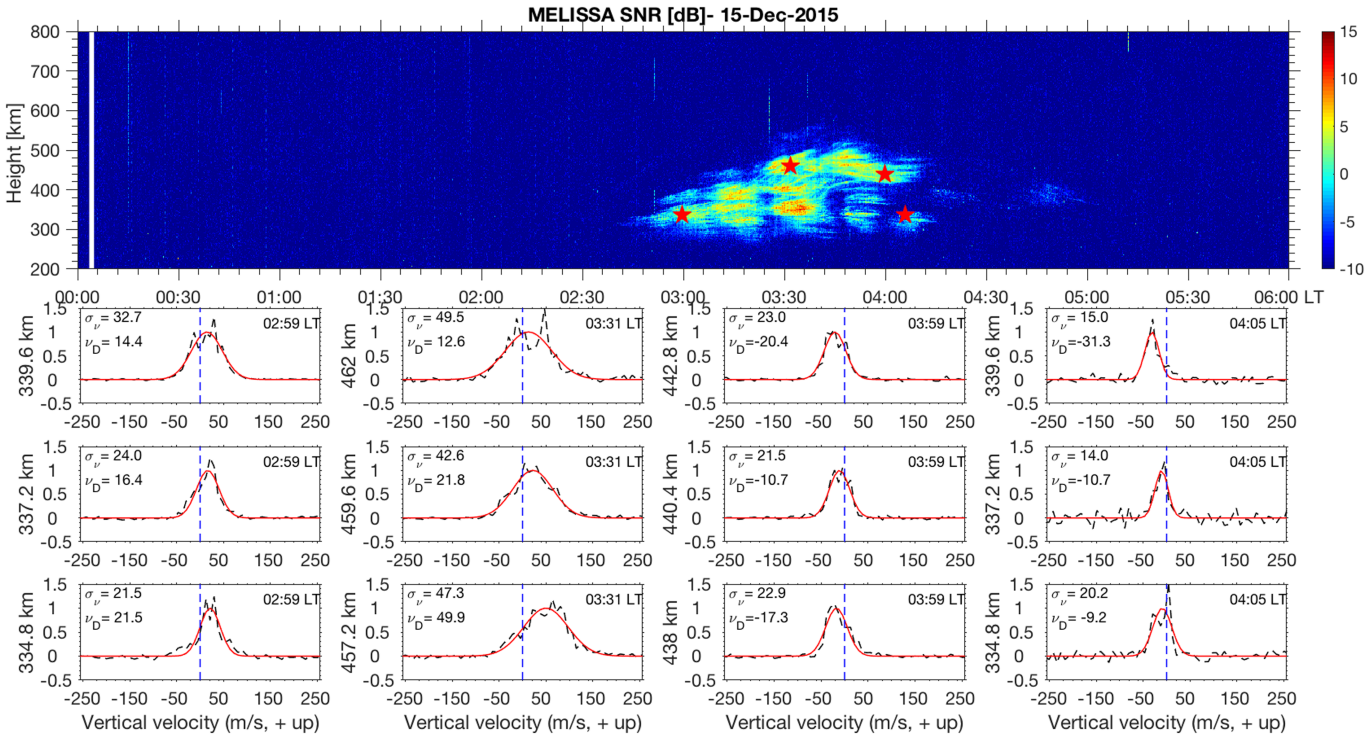

Figure 6. Same as Figure 4 but for 15 December 2015.

Around 02:00 LT, the echoes are weak and suggest the occurrence of fossil structures, which were created much earlier. The spectra (last column) show very narrow echoes, with spectral widths that are similar to those associated with decaying pre-midnight ESF (see Figure 4, fourth column of spectra). However, unlike the pre-midnight case, the mean Doppler velocities are near zero suggesting weak vertical background plasma drifts.

The digisonde data for this event, shown in Figure 9a, support the idea of destabilizing conditions around midnight, which could have led to a "fresh" ESF structure and the radar echoes seen around midnight. The digisonde data (h'F) show an apparent uplift of the *F*-layer starting around 23:00 LT on 28 December, about 30 min before the second group of late-night echoes start to be observed by MELISSA (see Figure 3). The base of the *F*-layer only descends around 02:00 LT. At that time radar echoes also ceased to be observed.

3.2.2. Strong Post-Midnight *F*-Region Echoes

Figure 6 now shows the second type of post-midnight echoes observed by MELISSA. The example is from observations made on 15 December 2015. Unlike the previous case, these post-midnight echoes appear away from the midnight sector. The intensity of the echoes (SNR) suggests that irregularities have recently been generated but, as proposed by this study, the spectral analyses can provide additional evidence of such a scenario.

Again, spectra for four distinct regions of the RTI map are shown in the bottom panels of Figure 6. In the first selected region, around the beginning of the event at 03:00 LT, the echoes have moderate spectral widths (20–30 m/s) and positive mean Doppler velocities. In the second region, from around 03:30 LT and a more developed echoing layer in the RTI map, the echoes show broader spectral widths (~40–50 m/s) and again, positive Doppler velocities. Mean Doppler velocities near 50 m/s can be observed. The last two selections come from the late phases of the event, around 04:00 and 04:05 LT. During that time, the echoes are weak and seemed to come from decaying irregularities. The spectra of these echoes show narrow widths (15–30 m/s) and negative (downward) mean Doppler velocities indicating the same conditions of echoes seen in the late phases of post-sunset ESF events.

The spectral features of this event suggest a structure developing over or near the São Luís site in the post-midnight hours. Similar to post-sunset events, the echoes start with positive mean Doppler velocities

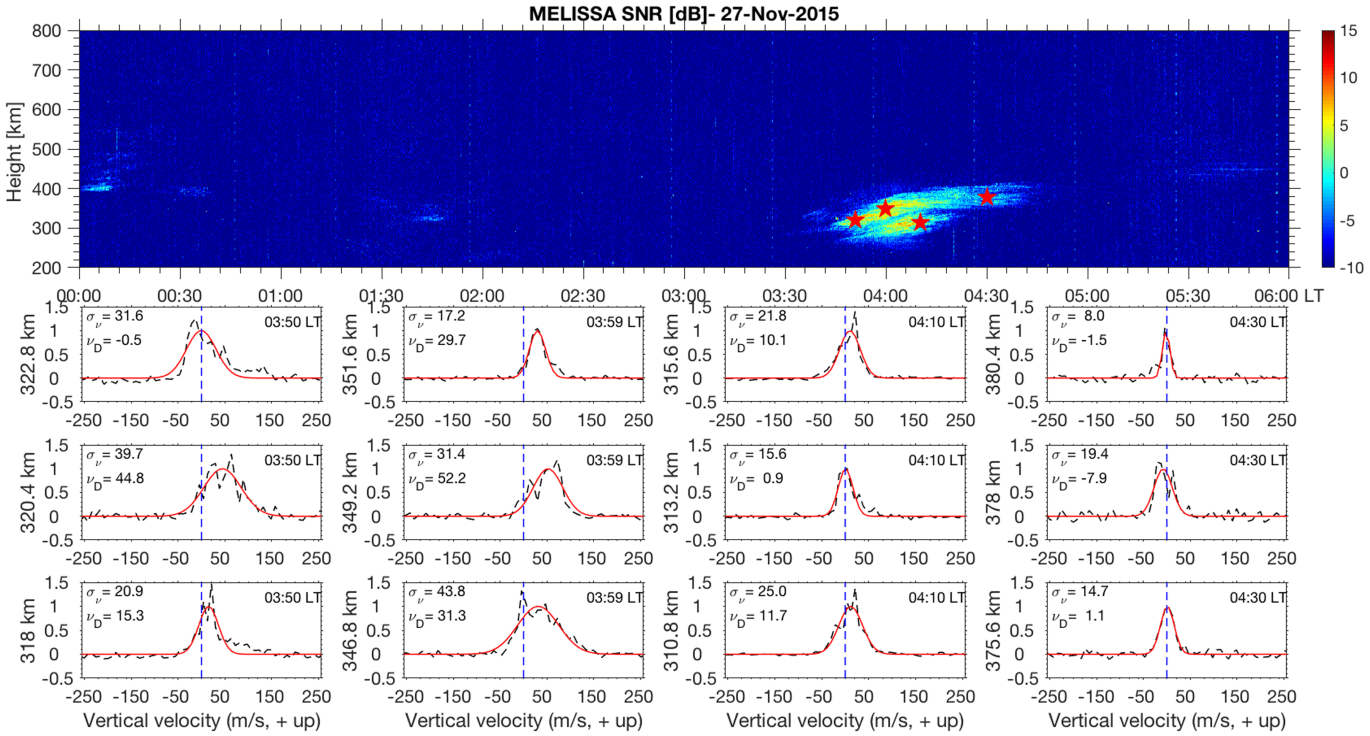

Figure 7. Same as Figure 4 but for 27 November 2015.

and broad spectral widths. Then the late echoes are narrow and show negative Doppler velocities following the expected behavior of the background plasma drifts based on climatological models.

Looking at the digisonde data for this day (Figure 9b) we can notice, again, an apparent uplift of the *F*-region starting around 02:00 LT, about 45 min before the first post-midnight echoes are detected. This uplift supports the idea of destabilizing conditions in the post-midnight sector and the generation of new irregularities causing the echoes that start to be seen around 02:45 LT.

Another example of observations showing relatively strong echoes in the post-midnight sector is shown in Figure 7. Analyses of the echoes show again cases of wide spectra in at least some of the range gates of the first two selected regions, from around 03:50 and 04:00 LT (first and second columns). The mean Doppler velocities are also positive. Later, around 04:10 and 04:30 LT the echoes are much narrower and with mean Doppler velocities much closer to 0 m/s. Again, the digisonde data (Figure 9c) shows small, but noticeable increases in h'F and hmF2 starting around 03:00 LT preceding the appearance of the echoes and irregularities by approximately 40 min.

3.2.3. Weak Post-Midnight *F*-Region Echoes

Finally, Figure 8 shows an example of very weak post-midnight echoes that one would be inclined to associate with fossil ESF structures, that is, with *F*-region irregularities that were generated at earlier times and outside the field-of-view of the radar, and that drifted into the field-of-view as they moved zonally with the background plasma. The first echoes start to be observed around 03:00 LT.

Our observations show, however, that the spectral features of the observed echoes do not match those of decaying irregularities, that is, mostly narrow widths and negative Doppler velocities. Instead, a number of the echoes show wide spectral widths (as large as 35.7 m/s) and spectra with positive mean velocities. See the examples of spectra shown in Figure 8.

The digisonde data (Figure 9(d)) confirms an *F*-region behavior that might favor the GRT instability growth. The bottomside *F*-region starts to increase around 01:30 LT, about 90 min prior to the appearance of the first echoes. At about 02:45 LT, the layer peak has reached ~275 km altitude, and the first echoes are seen in the RTI map. The layer remains high for the rest of the night, and the echoes continue to be observed.

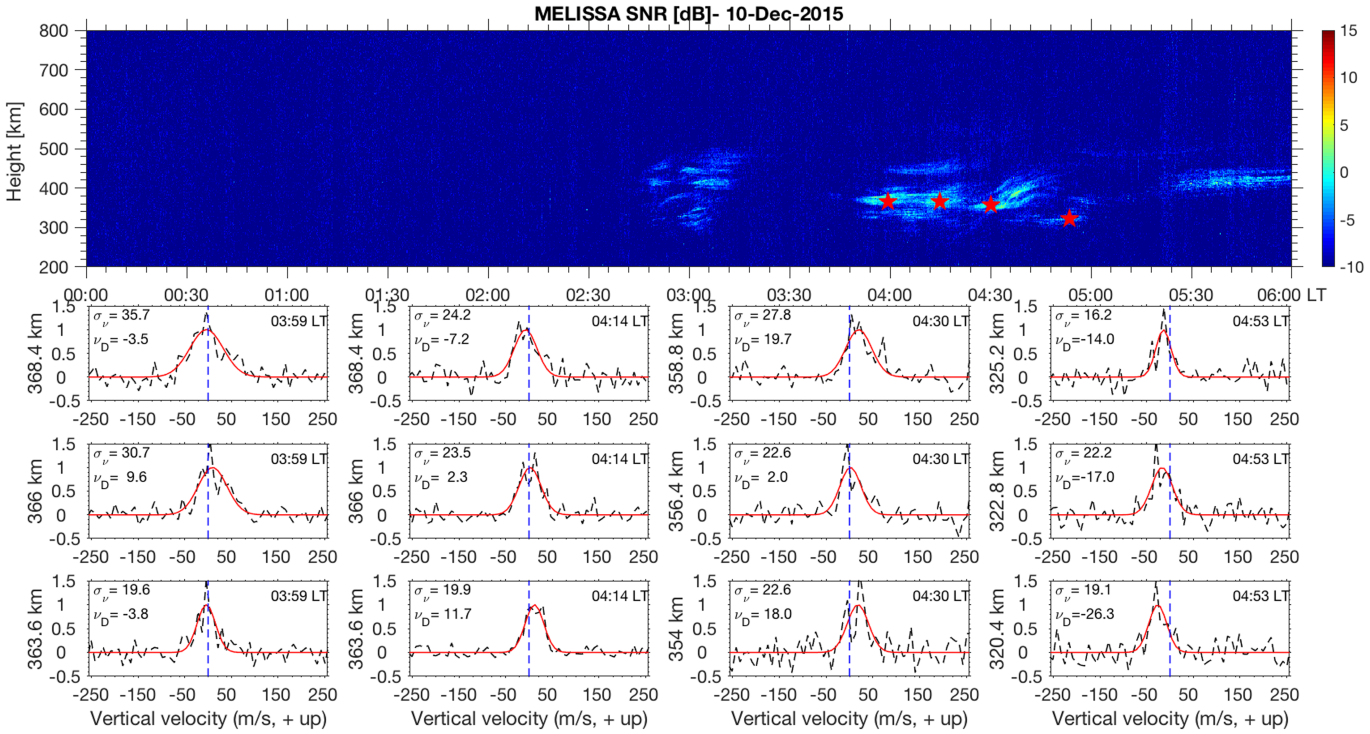

Figure 8. Same as Figure 4 but for 10 December 2015.

3.3. Potential Origin of the Observed Post-Midnight Uplifts

While not the main goal of this study, we also investigated a potential explanation for the occurrence of the *F*-region uplifts preceding the post-midnight irregularity events detected by the radar. We looked, particularly, on the role of disturbance electric fields of solar wind-magnetospheric origin.

Disturbances in the equatorial zonal electric fields (vertical **E**×**B** drifts) with time scales of a few hours have been attributed to the occurrence of nearly simultaneous enhancements in the electric fields observed at high latitudes (Fejer, 1981). These "prompt penetration" electric fields have been shown to oppose the regular pattern of equatorial upward drifts during the day and downward drifts at night. Additionally, large and long-lasting enhancements in the high-latitude electric fields have been observed to affect equatorial vertical drifts as well (Fejer, 1991). These high-latitude electric fields drive enhanced currents and Joule heating, which in turn affect the global circulation of thermospheric neutral winds as well as the ionospheric current system at mid- and low-latitudes. As a result, disturbances in the equatorial vertical plasma drifts are observed from a few to several hours after the beginning of the high-latitude enhancements.

To investigate the potential of disturbance electric fields, we followed the approach described and used by Scherliess and Fejer (1997) and more recently by Navarro et al. (2019). In that approach, the auroral electrojet (AE) index was used as a proxy of the magnitude of the electric fields (and currents) at high latitudes, and its time variation has been shown to correlate well with disturbances in the equatorial drifts. Figure 10 shows the local time variation of the AE index for each example discussed in the previous sections. The most striking feature is that the AE index shows significant high-latitude activity starting several hours prior to the occurrence of all the ESF events except the case when ESF was observed around midnight (top RTI map of Figure 10). This suggests the occurrence of significant Joule heating and disturbed dynamo winds that could have contributed to the generation of abnormal equatorial plasma drifts for the cases when irregularities were observed well after midnight.

It has been shown that the disturbed dynamo is very effective in driving upward drifts during nighttime hours, with the largest disturbed vertical drifts occurring around 03:00 LT (Navarro et al., 2019). Then the expected timing of disturbed drifts driven by high-latitude activity is in good agreement with our observations of post-midnight ESF, which started around 03:00 LT. Therefore, given the observations we are inclined to suggest that the *F*-region uplifts detected well after midnight were driven by disturbed dynamo electric

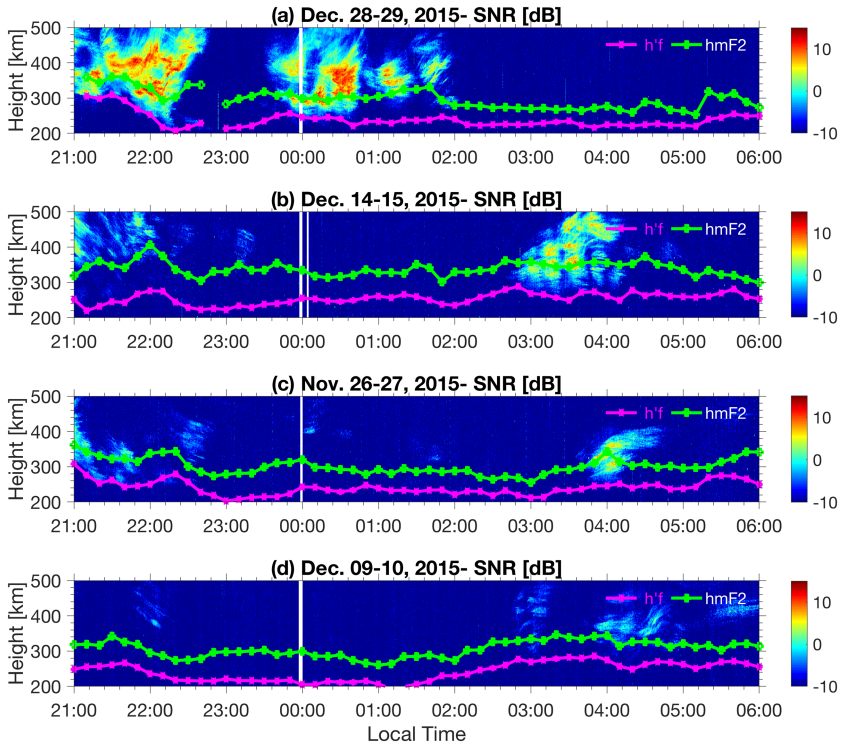

Figure 9. The local time variation of h'F and hmF2 for the ESF events discussed in this report. The digisonde parameters are superimposed on the RTI map for each case.

fields (vertical drifts). Despite being modest at most times, these drifts and *F*-region uplifts could have created conditions favorable to the GRT instability and to the development of the observed ESF events. This hypothesis is certainly more plausible during the low solar flux conditions under which our measurements were made. During those conditions the neutral atmosphere is more contracted, and even small uplifts might cause significant changes in the g/ν_{in} term (where g is the gravitational acceleration and ν_{in} is the ion-neutral collision frequency) in the linear growth rate of the GRT instability (Basu, 2002).

On 28–29 December 2015, when post-midnight echoes started to be detected around midnight, AE index variations were substantially smaller than those observed in the other examples (see Figure 10a). Nevertheless, the digisonde data (h'F) show an apparent uplift of the *F*-layer starting around 23:00 LT on 28 December, about 30 min prior to echoes being observed by MELISSA. For this case, we are left to suggest that quiet time variations in the vertical drifts led to destabilizing *F*-region conditions. An apparent *F*-region uplift and conditions favorable to the GRT instability growth can be produced, for instance, from weakening vertical drifts as suggested by Nicolls et al. (2006). Recent studies provide experimental evidence that weakening drifts can produce apparent uplifts starting in the pre-midnight sector and *F*-region irregularities during post-midnight hours (Ajith et al., 2016; Zhan & Rodrigues, 2018).

4. Summary

We presented a description of a 30 MHz coherent backscatter radar system that operated in the low-latitude site of São Luís (2.59°S, 44.21°W, 3.25°S dip latitude) in Brazil between March 2014 and December 2018. The system is referred to as Measurements of Equatorial and Low-latitude Ionospheric irregularities over São Luís, South America (MELISSA), and allowed observations of the *F*-region during pre- and post-midnight hours. The description of the system is followed by a quick summary of *F*-region measurements and presentation and discussion of observation examples.

This report focuses on presenting the spectral features of equatorial spread *F* (ESF) events observed by MELISSA. Despite the operation of the 30 MHz FCI radar in São Luís between 2001 and 2012, observations

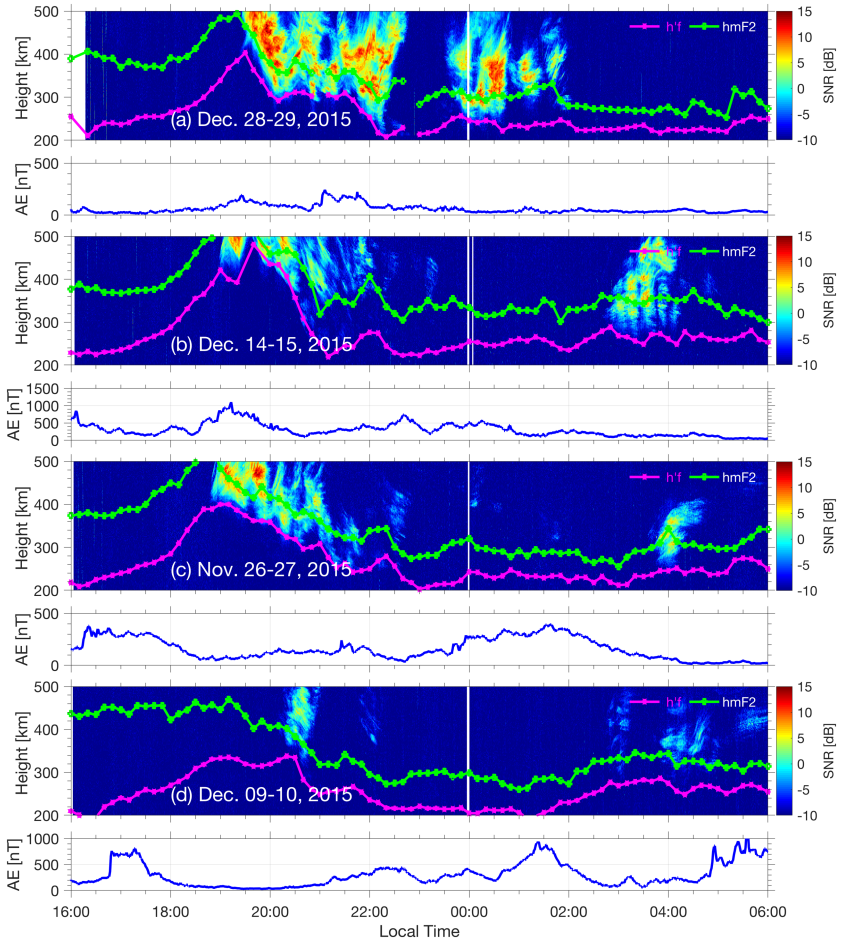

Figure 10. RTI maps of the post-midnight events examined in this study. On the RTI maps we also show again the behavior of h'F and hmF2. Below each RTI map we show the behavior of the Auroral Electrojet (AE) geomagnetic index several hours before the beginning of the post-midnight ESF events. Note that the range of the vertical axis for the AE index varies from case to case.

past local midnight were limited. Additionally, the spectral features of *F*-region echoes had yet to be presented. We showed examples of echoes observed by MELISSA during December Solstice 2015 when *F*-region irregularities were observed during pre- and post-midnight hours.

In addition to presenting the main features of the Doppler spectra of the echoes, we also investigated the potential of these features to provide additional information on the local time origin of the irregularities causing the echoes. Conventional (single beam) radar observations have been used to detect the occurrence of post-midnight ESF. While one is inclined to relate weak echoes to decaying irregularity structures, the signal intensity does not permit to determine, unambiguously, if echoes were caused by "fresh" or "fossil" ESF events. In order to better understand the lifetime stage of the observed echoes, we compared the spectral features of post-midnight ESF events to spectral features of typical, post-sunset ESF events. Similar to previous studies (Woodman & La Hoz, 1976), MELISSA observations show spectra that varies significantly from range gate to range gate specially during the early, developing stage of typical ESF events. The echoes are typically wide (>30 m/s) and with positive mean Doppler velocities. As time progresses and turbulence levels decrease, narrower echoes were observed accompanied by negative mean Doppler velocities.

A comparison of the spectral features of post-midnight echoes with those of post-sunset events suggests that the observed post-midnight *F*-region irregularities developed outside the evening sector, that is, in the late evening and post-midnight hours. This finding also includes cases where the echoes are weak and that could have been associated with "fossil" ESF events. Collocated digisonde observations support the inference from the radar observations The digisonde observations indicate modest but noticeable apparent *F*-region uplifts

preceding the ESF events. For some of the cases, the uplifts have been associated with abnormal vertical drifts driven by disturbed dynamo conditions. Apparent uplifts near midnight have also been observed during geomagnetically quiet conditions. The observations indicate that during low-solar flux conditions such as those under which the measurements were made, even modest uplifts might create favorable conditions for instability growth and ESF development.

Data Availability Statement

The RTI maps and data sets used in this study are available in a public repository (http://doi.org/10.5281/zenodo.3560118).

Acknowledgments
The development, deployment, and maintenance of the MELISSA system were supported by an AFOSR award (FA9550-13-1-0095) to UT Dallas. Work at UT Dallas was partially supported by NASA (80NSSC18K1203) and NSF (AGS-1554926). A. M. Santos acknowledges Fundação de Amparo à Pesquisa do Estado de São Paulo – FAPESP for financial support under grant 2015/25357-4. E.R. de Paula was partially supported by CNPq Process 310802/2015-6.

References

Abdu, M. A. (2016). Electrodynamics of ionospheric weather over low latitudes. *Geoscience Letters*, *3*, 11. https://doi.org/10.1186/s40562-016-0043-6

Abdu, M. A. (2019). Day-to-day and short-term variabilities in the equatorial plasma bubble/spread F irregularity seeding and development. *Progress in Earth and Planetary Science*, *6*(1), 2019.

Abdu, M. A., Denardini, C. M., Sobral, J. H. A., Batista, I. S., Muralikrishna, P., & de Paula, E. R. (2002). Equatorial electrojet irregularities investigations using a 50 MHz back-scatter radar and a digisonde at Sao Luis: Some initial results. *Journal of Atmospheric and Solar-Terrestrial Physics*, *64*(12–14), 1425–1434. https://doi.org/10.1016/S1364-6826(02)00106-2

Ajith, K. K., Tulasi Ram, S., Yamamoto, M., Otsuka, Y., & Niranjan, K. (2016). On the fresh development of equatorial plasma bubbles around the midnight hours of June solstice. *Journal of Geophysical Research: Space Physics*, *121*, 9051–9062. https://doi.org/10.1002/2016JA023024

Alam Kherani, E., Abdu, M. A., de Paula, E. R., Fritts, D. C., Sobral, J. H. A., & de Meneses Jr., F. C. (2009). The impact of gravity waves rising from convection in the lower atmosphere on the generation and nonlinear evolution of equatorial bubble. *Annales de Geophysique*, *27*, 1657–1668. https://doi.org/10.5194/angeo-27-1657-2009

Aveiro, H. C., & Hysell, D. L. (2010). Three-dimensional numerical simulation of equatorial F region plasma irregularities with bottomside shear flow. *Journal of Geophysical Research*, *115*, A11321. https://doi.org/10.1029/2010JA015602

Basu, B. (2002). On the linear theory of equatorial plasma instability: Comparison of different descriptions. *Journal of Geophysical Research*, *107*, A81199. https://doi.org/10.1029/2001JA000317

Basu, S., MacKenzie, E., & Basu, S. (1988). Ionospheric constraints on VHF/UHF communications links during solar maximum and minimum periods. *Radio Science*, *23*(3), 363–378. https://doi.org/10.1029/RS023i003p00363

Booker, H. G., & Wells, H. W. (1938). Scattering of radio waves by the F-region of the ionosphere. *Terrestrial Magnetism and Atmospheric Electricity*, *43*(3), 249–256. https://doi.org/10.1029/TE043i003p00249

Candido, C. M. N., Batista, I. S., Becker-Guedes, F., Abdu, M. A., Sobral, J. H. A., & Takahashi, H. (2011). Spread F occurrence over a southern anomaly crest location in Brazil during June solstice of solar minimum activity. *Journal of Geophysical Research*, *116*, A06316. https://doi.org/10.1029/2010JA016374

Carrano, C. S., Groves, K. M., & Caton, R. G. (2012). Simulating the impacts of ionospheric scintillation on L band SAR image formation. *Radio Science*, *47*, RS0L20. https://doi.org/10.1029/2011RS004956

de Paula, E. R., & Hysell, D. L. (2004). The São Luís 30 MHz coherent scatter ionospheric radar: System description and initial results. *Radio Science*, *39*, RS1014. https://doi.org/10.1029/2003RS002914

Fejer, B. G. (1981). The equatorial ionospheric electric fields: A review. *Journal of Atmospheric and Terrestrial Physics*, *43*(5/6), 377–386. https://doi.org/10.1016/0021-9169(81)90101-X

Fejer, B. G. (1991). Low latitude electrodynamic plasma drifts: A review. *Journal of Atmospheric and Terrestrial Physics*, *53*(8), 677–693. https://doi.org/10.1016/0021-9169(91)90121-M

Fejer, B. G., Scherliess, L., & de Paula, E. R. (1999). Effects of the vertical plasma drift velocity on the generation and evolution of equatorial spread F. *Journal of Geophysical Research*, *104*(A9), 19,859–19,869. https://doi.org/10.1029/1999JA900271

Fukao, S., McClure, J. P., Ito, A., Sato, T., Kimura, I., Tsuda, T., & Kato, S. (1988). First VHF radar observation of mid- latitude F-region field-aligned irregularities. *Geophysical Research Letters*, *15*(8), 768–771.

Harding, B. J., & Milla, M. (2013). Radar imaging with compressed sensing. *Radio Science*, *48*, 582–588. https://doi.org/10.1002/rds.20063

Huang, C., & Hairston, M. R. (2015). The postsunset vertical plasma drift and its effects on the generation of equatorial plasma bubbles observed by the C/NOFS satellite. *Journal of Geophysical Research: Space Physics*, *120*, 2263–2275. https://doi.org/10.1002/2014JA020735

Hysell, D. L., & Burcham, J. D. (2002). Long term studies of equatorial spread F using the JULIA radar at Jicamarca. *Journal of Atmospheric and Solar - Terrestrial Physics*, *64*(12–14), 1531–1543. https://doi.org/10.1016/S1364-6826(02)00091-3

Hysell, D. L., & Chau, J. L. (2006). Optimal aperture synthesis radar imaging. *Radio Science*, *41*, RS2003. https://doi.org/10.1029/2005RS003383

Kintner, P. M., Ledvina, B. M., & de Paula, E. R. (2007). GPS and ionospheric scintillations. *Space Weather*, *5*, S09003. https://doi.org/10.1029/2006SW000260

Navarro, L. A., Fejer, B. G., & Scherliess, L. (2019). Equatorial disturbance dynamo vertical plasma drifts over Jicamarca: Bimonthly and solar cycle dependence. *Journal of Geophysical Research: Space Physics*, *124*, 4833–4841. https://doi.org/10.1029/2019JA026729

Nicolls, M. J., Kelley, M. C., Vlasov, M. N., Sahai, Y., Chau, J. L., Hysell, D. L., et al. (2006). Observations and modeling of post-midnight uplifts near the magnetic equator. *Annales Geophysicae*, *24*, 1317–1331. https://doi.org/10.5194/angeo-24-1317-2006

Ning, B., Hu, L., Li, G., et al. (2012). The first time observations of low-latitude ionospheric irregularities by VHF radar in Hainan. *Science China Technological Sciences*, *55*, 1189. https://doi.org/10.1007/s11431-012-4800-2

Otsuka, Y. (2018). Review of the generation mechanisms of post-midnight irregularities in the equatorial and low-latitude ionosphere. *Progress in Earth and Planetary Science*, *5*, 57. https://doi.org/10.1186/s40645-018-0212-7

Otsuka, Y., Ogawa, T., & Effendy (2009). VHF radar observations of nighttime F-region field-aligned irregularities over Kototabang Indonesia. *Earth, Planets and Space*, *61*, 431. https://doi.org/10.1186/BF03353159

Patra, A. K., Anandan, V. K., Rao, P. B., & Jain, A. R. (1995). First observations of equatorial spread F from Indian MST radar. *Radio Science*, *30*(4), 1159–1165. https://doi.org/10.1029/95RS00650

Patra, A. K., Rao, P. B., Anandan, V. K., & Jain, A. R. (1997). Radar observations of 2.8 m equatorial spread-F irregularities. *Journal of Atmospheric and Solar-Terrestrial Physics*, *59*(13), 1633–1641. https://doi.org/10.1016/S1364-6826(96)00162-9

Rodrigues, F. S., de Paula, E. R., Abdu, M. A., Jardim, A. C., Iyer, K. N., Kintner, P. M., & Hysell, D. L. (2004). Equatorial spread F irregularity characteristics over São Luís, Brazil, using VHF radar and GPS scintillation techniques. *Radio Science*, *39*, RS1S31. https://doi.org/10.1029/2002RS002826

Rodrigues, F. S., de Paula, E. R., & Zewdie, G. K. (2017). High-resolution coherent backscatter interferometric radar images of equatorial spread F using Capon's method. *Annales de Geophysique*, *35*, 393–402. https://doi.org/10.5194/angeo-35-393-2017

Rodrigues, F. S., Hysell, D. L., & de Paula, E. R. (2008). Coherent backscatter radar imaging in Brazil: Large-scale waves in the bottomside F-region at the onset of equatorial spread F. *Annales de Geophysique*, *26*, 3355–3364. https://doi.org/10.5194/angeo-26-3355-2008

Scherliess, L., & Fejer, B. G. (1997). Storm time dependence of equatorial disturbance dynamo zonal electric fields. *Journal of Geophysical Research*, *102*(A11), 24,037–24,046. https://doi.org/10.1029/97JA02165

Smith, J. M., Rodrigues, F. S., Fejer, B. G., & Milla, M. A. (2016). Coherent and incoherent scatter radar study of the climatology and day-to-day variability of mean F region vertical drifts and equatorial spread F. *Journal of Geophysical Research: Space Physics*, *121*, 1466–1482. https://doi.org/10.1002/2015JA021934

Sobral, J. H. A., Abdu, M. A., Takahashi, H., Taylor, M. J., de Paula, E. R., Zamlutti, C. J., et al. (2002). Ionospheric plasma bubble climatology over Brazil based on 22 years (1977–1998) of 630 nm airglow observations. *Journal of Atmospheric and Solar - Terrestrial Physics*, *64*(12-14), 1517–1524. https://doi.org/10.1016/S1364-6826(02)00089-5

Sultan, P. J. (1996). Linear theory and modeling of the Rayleigh-Taylor instability leading to the occurrence of equatorial spread F. *Journal of Geophysical Research*, *101*(A12), 26,875–26,891. https://doi.org/10.1029/96JA00682

Swartz, W. E., & Woodman, R. F. (1998). Same night observations of spread-F by the Jicamarca Radio Observatory in Peru and CUPRI in Alcantara, Brazil. *Geophysical Research Letters*, *25*(1), 17–20. https://doi.org/10.1029/97GL03484

Tsunoda, R. T., Baron, M. J., Owen, J., & Towle, D. M. (1979). Altair: An incoherent scatter radar for equatorial spread F studies. *Radio Science*, *14*(6), 1111–1119. https://doi.org/10.1029/RS014i006p01111

Tsunoda, R. T., Bubenik, D. M., Thampi, S. V., & Yamamoto, M. (2010). On large-scale wave structure and equatorial spread F without a post-sunset rise of the F layer. *Geophysical Research Letters*, *37*, L07105. https://doi.org/10.1029/2009GL042357

Woodman, R., & La Hoz, C. (1976). Radar observations of F region equatorial irregularities. *Journal of Geophysical Research*, *81*(31), 5447–5466. https://doi.org/10.1029/JA081i031p05447

Woodman, R. F. (1985). Spectral moment estimation in MST radars. *Radio Science*, *20*(6), 1185–1195. https://doi.org/10.1029/RS020i006p01185

Woodman, R. F. (2009). Spread F—An old equatorial aeronomy problem finally resolved? *Annales de Geophysique*, *27*, 1915–1934. https://doi.org/10.5194/angeo-27-1915-2009

Yizengaw, E., Retterer, J., Pacheco, E. E., Roddy, P., Groves, K., Caton, R., & Baki, P. (2013). Postmidnight bubbles and scintillations in the quiet-time June solstice. *Geophysical Research Letters*, *40*, 5592–5597. https://doi.org/10.1002/2013GL058307

Zalesak, S. T., Ossakow, S. L., & Chaturvedi, P. K. (1982). Nonlinear equatorial spread F: The effect of neutral winds and background Pedersen conductivity. *Journal of Geophysical Research*, *87*(A1), 151. https://doi.org/10.1029/JA087iA01p00151

Zhan, W., & Rodrigues, F. S. (2018). June solstice equatorial spread F in the American sector: A numerical assessment of linear stability aided by incoherent scatter radar measurements. *Journal of Geophysical Research: Space Physics*, *123*, 755–767. https://doi.org/10.1002/2017JA024969